RHS-to-RHS COLD-FORMED S960 STEEL FIRE EXPOSED X-JOINTS: STRUCTURAL BEHAVIOUR AND DESIGN

Madhup Pandey[1,*] and Ben Young[2]

[1]*Department of Civil Engineering, University of Nottingham, Nottingham, United Kingdom.*
[2]*Department of Civil and Environmental Engineering, The Hong Kong Polytechnic University, Hong Kong, China.*

Abstract

This paper presents a detailed finite element (FE) analysis and design of cold-formed high strength steel (CFHSS) fire exposed X-joints with square and rectangular hollow section (SHS and RHS) brace and chord members. The nominal 0.2% proof stress of SHS and RHS (henceforth, RHS includes SHS) members was 960 MPa. The static behaviour of RHS X-joints was numerically investigated corresponding to 4 post-fire temperatures, including 300°C, 550°C, 750°C and 900°C. The RHS X-joints were subjected to axial compression loads through brace members. The post-fire residual strengths of cold-formed S960 steel grade RHS X-joints were experimentally investigated by the authors. The test results were used to develop an accurate FE model. Through the validated FE model, a comprehensive FE parametric study comprising of 756 FE specimens was performed in this investigation. Overall, RHS X-joint specimens were failed by chord face failure, chord side wall failure and a combination of these two failure modes. The validity ranges of critical geometric parameters were extended beyond current limits mentioned in international codes and guides. Using the measured post-fire residual static material properties, nominal resistances were predicted from design rules given in Eurocode 3, CIDECT and literature. The residual joint strengths of test and FE specimens were compared with predicted nominal resistances. Generally, it has been shown that the existing design rules are quite conservative but unreliable. As a result, accurate and reliable design rules are proposed in this study.

Keywords: Cold-formed steel; Design equations; FE analysis; High strength steel; Post-fire; tubular joints.

*Corresponding author. (e-mail: madhup.pandey@nottingham.ac.uk).

1. Introduction

Over the past few decades, structures have become increasingly vulnerable to fires. The failure of structures in the September 11 incident got the attention of worldwide researchers. Knowing the adverse influence of fire that leads to the sudden or progressive collapse of a structure, the compliance of ensuring adequate structural resistance at peak fire temperature has now become one of the critical structural design considerations. However, a fire exposed structure that survived its peak fire temperature could not be considered safe for its direct reuse. The shrinkage residual stresses developed during the cooling phase could be quite detrimental compared to the member stresses at the peak fire temperature. Therefore, it is imperative to carry out a post-fire investigation before a fire exposed structure is allowed for its reuse.

Due to various merits of hollow section members, including high torsional strength, superior aesthetical appearance, ability to confine in-filled material and so on, tubular members are commonly used in both onshore and offshore structures. Although several investigations were carried out in the last six decades to investigate the static behaviour of different types of tubular joints, however, investigations dealing with the post-fire behaviour of tubular joints largely remain scant. The post-fire behaviour of circular hollow section (CHS) T-joints made of Q345B steel grade was investigated by Jin et al. [1]. It was concluded that the effect of preload on the residual capacities of fire exposed CHS T-joints was trivial. Experimental and numerical studies were carried out by Gao et al. [2] to investigate the cyclic performance of fire exposed CHS T-joints made of normal strength steel (in this study, refer to steels with steel grades less than or equal to S460). The CHS T-joints were reinforced with doubler plates. The energy dissipation capacities of CHS T-joints were significantly reduced after fire exposures. The post-fire behaviour of concrete in-filled CHS T-joints was experimentally and numerically investigated by Gao et al. [3]. It was found that the residual capacities of fire exposed concrete in-filled CHS T-joints were less than the corresponding fire exposed hollow CHS T-joints. Pandey and Young [4] carried out tests to investigate the residual strengths ($N_{f,\psi}$) of ISO-834 [5] fire exposed cold-formed S900 and S960 steel grades square and rectangular hollow section (SHS and RHS) T- and X-joints. Except these studies, to the best of the authors' knowledge, no other investigation is available on the post-fire behaviour of normal and high strength steel tubular joints. In this paper, high strength steel (HSS) refers to steels with steel grades higher than S460.

An extensive numerical investigation was performed in this study to investigate the residual strengths ($N_{f,\psi}$) of cold-formed high strength steel (CFHSS) fire exposed X-joints made of RHS (henceforth, RHS includes SHS) brace and chord members. The test results reported in Pandey and Young [4] were used to develop an accurate finite element (FE) model in this study. Using the developed FE model, a total of 756 FE X-joint specimens were analysed in the numerical parametric study. The residual strengths ($N_{f,\psi}$) of test [4] and FE X-joint specimens were compared with the nominal resistances predicted from design rules given in EC3 [6], CIDECT [7] and literature [8,9]. Commonly, it has been demonstrated that the existing design rules are quite conservative but unreliable for the range of fire exposed RHS X-joints investigated in this study. Therefore, using two design methods, accurate and reliable design equations are proposed in this study to predict the $N_{f,\psi}$ of cold-formed S960 steel grade RHS X-joints subjected to post-fire temperatures ranging from 300°C to 900°C.

2. Outline of experimental investigation

The static behaviour of CFHSS fire exposed T- and X-joints was investigated by Pandey and Young [4]. Before conducting the static joint tests, the test specimens were subjected to a total of three fire exposures. The preselected peak temperatures (ψ) of three fire exposures were 300°C, 550°C and 750°C, respectively. In total, 9 X-joints made of RHS braces and chords were fabricated. The thermo-mechanically controlled processed plates of S960 steel grade were cold-formed to obtain hollow section members. The nominal 0.2% proof stress of without fire exposed RHS members was 960 MPa. The braces and chords were welded using robotic metal active gas welding. The test specimens were equally grouped in 3 batches for the 3 fire exposures (i.e. ψ_1=300°C, ψ_2=550°C and ψ_3=750°C). All 3 batches of test specimens were exposed to fire inside a gas furnace, where the furnace temperature was increased in accordance with ISO-834 [5]. After attaining the preselected peak temperatures (ψ), the test specimens were allowed to naturally cool inside the furnace. Subsequently, at room temperature, X-joint test specimens were axially compressed through brace members. Fig. 1 presents various notations for RHS X-joint. The static behaviour of RHS X-joint primarily depends on few geometric ratios, including β (b_1/b_0), τ (t_1/t_0), 2γ (b_0/t_0) and h_0/t_0. The symbols b, h, t and R stand for cross-section width, depth, thickness and external corner radius of RHS member, respectively. The subscripts 0 and 1 represent chord and brace, respectively. In the experimental investigation [4], β varied from 0.41 to 1.0, τ varied from 0.98 to 1.01, 2γ varied from 30.8 to 35.2 and h_0/t_0 varied from 30.9 to 35.6.

The lengths of braces (L_1) were equal to two times the maximum of b_1 and h_1. On the other hand, the lengths of chords (L_0) were equal to $h_1 + 3h_0$. The test results were obtained in the form of

$N_{f,\psi}$ vs u and $N_{f,\psi}$ vs v curves, where $N_{f,\psi}$, u and v respectively stand for residual load, chord face indentation and chord side wall deformation. It should be noted that $N_{f,\psi}$ vs u curves were used to determine the $N_{f,\psi}$ of fire exposed RHS X-joints. The testing machine was paused for 120 seconds at two different locations in each test. The load drops captured during the pauses were used to convert test curves into static curves. Consequently, the obtained test results were free from the influence of the applied loading rate. The test results are detailed in Pandey and Young [4]. The material properties of ISO-834 [5] fire exposed S900 and S960 steel grades tubular members were investigated by Pandey and Young [10] for post-fire temperature ranging from 300°C to 900°C. The test specimens in the experimental program [4] were fabricated from tubular members that belonged to the same batch of tubes used in Pandey and Young [10]. Thus, the material properties of fire exposed RHS members can be referred to Pandey and Young [10]. It should be noted that the cold-formed S960 steel grade RHS X-joints [4] and tubular members [10] were simultaneously exposed to fire inside the gas furnace. In addition to the 3 fire exposures (ψ_1=300°C, ψ_2=550°C and ψ_3=750°C) used in the investigation of the post-fire behaviour of RHS X-joints [4], the material properties of RHS members belonging to the identical mill batch were also investigated at 900°C (i.e. ψ_4=900°C) in Pandey and Young [10]. The measured values of static yield strength of fire exposed tubular members ranged from 1088 to 1145 MPa for ψ_1=300°C, 894 to 1023 MPa for ψ_2=550°C, 653 to 781 MPa for ψ_3=750°C and 310 to 347 MPa for ψ_4=900°C [10]. In the test program [10], coupon specimens were extracted after fire exposed tubular members cooled down to ambient temperature. As a result, the strength deterioration caused by the fire exposures was included. It is also important to note that the fire exposed tubular members in the test programs [4,10] were cooled down very slowly inside a closed furnace (i.e. furnace cooling). Due to this cooling approach, the impact of restored residual stresses on material strength was far lesser compared to air and water cooling approaches. The controlled heating and cooling inside a furnace can be regarded as hot-stress relieve method, which is performed on metal products to minimise residual stresses in the member. A slow cooling speed is important to avoid tensions caused by temperature differences in the material. It is important to note that, in this study, tensile stress-strain curves of coupon specimens extracted from the longitudinal direction of tubular members were used in the FE analyses. The developed FE models successfully replicated the joint resistance, failure mode and overall load vs deformation curves.

3. Numerical program

3.1. Finite element (FE) model of RHS X-joints

3.1.1. General

ABAQUS [11] was used to perform comprehensive FE analyses in this study. The static (general) analysis procedure given in ABAQUS [11] was used as the solver. As the induced strains in the FE model during the applied load were unidirectional (i.e. no load reversal), the isotropic strain hardening law was selected for the analysis. The von-Mises yield criterion is generally the default criterion used to predict the onset of yielding in most metals, except for porous metals. Therefore, the yielding onsets of FE models in this study were based on the von-Mises yield theory. In the FE analyses, the growth of the time step was kept non-linear in order to reduce the overall computation time. Furthermore, the default Newton-Raphson method was used to find the roots of non-linear equilibrium equations. In addition to the accuracy associated with the Newton-Raphson method, one of the other benefits of using this numerical technique is its quadratic convergent approach, which in turn significantly increases the convergence rate of non-linear problems.

The material non-linearities were considered in the FE models by assigning the measured values of post-fire residual static stress-strain curves of flat and corner portions of RHS members. However, experimentally obtained constitutive material curves were transformed into true stress-strain curves prior to their inclusion in the FE models. On the other hand, the geometric non-linearities in FE models were considered by enabling the non-linear geometry parameter (*NLGEOM) in ABAQUS [11], which allowed FE models to undergo large displacement during the analyses. Furthermore, various parameters, including through-thickness division, contact interactions, mesh seed spacing, corner region extension and element types, were also studied and reported in the following sub-sections of this paper. The labelling of parametric FE specimens was kept identical to the label system used in the test program [4]. Fig. 2 presents typical FE X-joint specimens modelled in this study.

3.1.2. Element type, mesh spacing and material properties

Except for the welds, all other parts of the FE models were developed using second-order hexahedral elements, particularly using the C3D20 elements. On the other hand, the second-order tetrahedral element, C3D10, was used to model the weld parts due to their complicated shapes. The weld parts were freely meshed using the free-mesh algorithm, however, brace and chord parts were meshed using the structure-mesh algorithm. The use of solid elements helped in making realistic fusions between tubular and weld parts of FE models. Convergence studies were conducted using different mesh sizes, and finally, chord and brace members were seeded at 4 mm and 7 mm intervals, respectively, along their corresponding longitudinal and transverse directions. Moreover, the seeding spacings of weld parts reciprocated the seeding spacings of their respective brace parts.

In order to assure the smooth transfer of stresses from flange to web regions, the corner portions of RHS were split into ten elements. FE analyses were also conducted to examine the influence of divisions along the wall thickness (*t*) of RHS members. The results of these FE analyses demonstrated the trivial influence of wall thickness divisions on the load vs deformation curves of the investigated RHS X-joints. The use of the C3D20 element having one built-in node along the thickness direction as well as the small wall thickness of test specimens (i.e. $t = 4$ mm) led to such observations. The presence of a built-in node naturally provides one division along the wall thickness of tubular members (i.e. two layers). It is worth noting that similar findings were also obtained in other studies [12-14]. Thus, for the validation of FE model, the wall thickness of tubular members was not divided. The measured post-fire static stress-strain curves of longitudinal flat and corner coupons of RHS members [10] were used in the FE models. In this study, the influence of cold-working was included in the FE models by assigning wider corner regions. Various distances for corner extension were investigated in this study. FE runs were performed by varying the corner extension regions from $1t$ to $3t$ into the neighbouring flat regions, and finally, the corner regions were extended by $2t$. Using this value, load-deformation curves from FE predictions matched relatively better with the corresponding test curves. In addition, the corner extension of $2t$ aligns well with other studies conducted on CFHSS tubular members and joints [12,13,15-17].

3.1.3. Modelling of welds and contact interaction definition

The welds were modelled in all FE specimens using the average values of measured weld sizes reported in Pandey and Young [4]. The fillet weld was modelled for FE specimens with β = 0.41, 0.42 and 0.57. However, when β = 1.0, groove and fillet welds (GW and FW) were respectively modelled along the length and width of the chord members. The HSS tubular members used in the tests [4] generally had large corner radii. It was, therefore, practically not feasible to maintain the roundness (or continuity) at corner regions during the welding process. As a result, welding of brace to chord was split into four steps, including one step for each face. The weld parts modelled in this study were consistent with the test program [4]. The inclusions of weld geometries appreciably improved the overall accuracies of FE models. In addition, modelling of weld parts helped attain realistic load transfer between brace and chord members, which facilitated in obtaining the actual joint behaviour. The selection of the C3D10 element maintained optimum stiffness around the joint perimeter due to its ability of taking complicated shapes.

A contact interaction was defined between brace and chord members of the FE model. In addition, a tie constraint was also established between the weld and tubular members of the FE model. The contact interaction was established using the built-in surface-to-surface contact definition. The contact interaction between brace and chord members of FE models was kept frictionless. Along the normal direction of the contact interaction, a 'hard' contact pressure overclosure was used. In addition, finite sliding was permitted between the interaction surfaces. It is worth noting that hard contact pressure-overclosure effectively transferred the tensile stresses along the weld-to-tubular member interfaces without any detachments. For both contact interaction and tie constraint, the surfaces were connected to each other using the 'master-slave' algorithm technique. This technique permits the separation of fused surfaces under tension, however, it does not allow penetration of fused surfaces under compression. For the brace-chord interaction, the cross-section surfaces of the braces connected to the chord member were assigned as the 'master' regions (relatively less deformable), while the chord connecting surfaces were assigned as the 'slave' regions (relatively more deformable). For the weld-tubular member tie connection, the weld surfaces were assigned as the 'master' regions, while the connecting brace and chord surfaces were assigned as the 'slave' regions.

3.1.4. Boundary conditions and load application

In order to assign boundary conditions in FE model, two reference points were created. The top and bottom reference points (TRP and BRP) were created at the cross-section centre of brace members, as shown in Fig. 2. Subsequently, TRP and BRP were coupled to their respective brace end cross-section surfaces using the kinematic coupling type. In order to exactly replicate the test setup, all degrees of freedom (DOF) of TRP were restrained. On the other hand, except for translation along the height of the specimen, all other DOF of BRP were also restrained. Moreover, all DOF of other nodes of FE specimen were kept unrestrained for rotation and translation. Using the displacement control method, compression load was then applied at the BRP of FE model. In addition, the size of the step increment was kept small in order to obtain smooth load vs deformation curves. Following this approach, the boundary conditions and load application in FE analyses were identical to those used in the test program [4].

3.1.5. Geometric imperfection in chord webs

Garifullin et al. [18] studied the influence of geometric imperfections on the behaviour of cold-formed steel hollow section joints. The imperfection profiles of RHS joints were obtained by performing elastic buckling analyses. The BUCKLE command of ABAQUS [11] was used to implement this methodology. The first mode of elastic buckling analysis of the FE specimen was treated as the imperfection mode of that specimen. The deformation scale of the first buckling mode was then ramped up to match the tolerance limits given in EN [19], which ranged from ± 0.6% to ± 1.0% of the outside tubular member dimensions. The scaled eigenmode shape was then superimposed on the FE model. Garifullin et al. [18] concluded the trivial influence of geometric imperfections on the static behaviour of hollow section joints. However, Pandey et al. [12] reported that the maximum measured values of cross-section width and depth of RHS members were on an average 2.9% more than their respective nominal dimensions. As tubular members used in the post-fire investigation of RHS X-joints [4] also belonged to the identical batch of tubes used in Refs. [12,20], therefore, it was necessary to model this geometric imperfection as an outward bulging 3-point convex arc, as shown in Fig. 3.

As all failure modes in tests [20,21] and numerical investigations [12,13] were only governed by the deformation of chord members, therefore, Pandey et al. [12,13] numerically examined the influence of outward bulging of chord cross-section on the static behaviour of hollow section joints. Finally, it was concluded that the effect of convex bulging of chord cross-section was only significant for equal-width (i.e. β=1.0) RHS joints. As a result, in this investigation, geometric imperfections were introduced as a 3-point convex arc in the chord webs of equal-width RHS X-joints. For the validation of FE models, the 3-point convex arc in the chord webs of equal-width RHS X-joints was modelled using the measured values of maximum chord cross-section widths (b_0) of such X-joints.

3.2. Validation of FE model

The FE model of CFHSS fire exposed RHS X-joint was developed using the modelling techniques described in the preceding section of this paper. The test results of RHS X-joints reported in Pandey and Young [4] were used to develop the FE model. The validation was performed by comparing the residual strengths ($N_{f,\psi}$), load vs deformation histories and failure modes of test and FE specimens. The measured dimensions of tubular members and welds were used to develop all FE models. In addition, measured post-fire residual static material properties of tubular members were used in the validation process. The residual strengths ($N_{f,\psi}$) of X-joint test specimens were compared with those predicted from their corresponding FE model (N_{FE}) in Table 1. The mean (P_m) and coefficients of variation (COV) (V_p) of the comparison are 1.00 and 0.006, respectively. It is worth mentioning that both ultimate load and 3% deformation limit load were used to determine the $N_{f,\psi}$ of test and FE specimens. In addition, load vs deformation curves were compared between test and FE specimens, as shown in Figs. 4 and 5. Furthermore, Figs. 6 and 7 present comparisons of distinct failure modes between typical test and FE specimens. Thus, the verified FE model precisely replicated the overall static behaviour of CFHSS fire exposed RHS X-joints, as shown in Table 1 and Figs. 4-7.

3.3. Parametric study

3.3.1. General

In order to gain a broad understanding of various governing factors affecting the static behaviour of CFHSS fire exposed RHS X-joints, the database was widened by performing a comprehensive numerical parametric study using the validated FE model. In the parametric study, 4 fire exposures with peak temperatures (ψ) equal to 300°C, 550°C, 750°C and 900°C were investigated, which were consistent with the test programs [4,10]. In total, 756 FE analyses were performed in the parametric study, including 189 FE analyses corresponding to each fire exposure. The validity ranges of important geometric ratios were purposefully widened beyond the present limitations set by EC3 [6] and CIDECT [7]. Table 2 presents the overall ranges of various critical parameters considered in the parametric study. In the parametric study, all FE modelling techniques described earlier in this paper were used.

3.3.2. Details of FE modelling

In the numerical investigation, the dimensions of RHS members included practical sizes. Overall, the values of cross-section width and depth of braces and chords of parametric FE specimens varied from 30 mm to 600 mm, while the wall thickness of braces and chords varied from 2.25 mm to 12.5 mm. The external corner radii of braces and chords (R_1 and R_0) conformed to commercially produced HSS members [22]. In this study, R_1 and R_0 were kept as 2t for $t \leq 6$ mm, 2.5t for $6 < t \leq 10$ mm and 3t for $t > 10$ mm, which in turn also meet the limits detailed in EN [19]. The formulae used to determine the lengths of braces and chords of parametric FE specimens were identical to those adopted in the test program [4], as detailed in Section 2 of this paper. For meshing along the longitudinal and transverse directions of tubular members, seedings were approximately spaced at the minimum of b/30 and h/30. Overall, the adopted mesh sizes of parametric FE specimens varied from 3 mm to 12 mm. On the other hand, the seeding interval of weld parts of parametric FE specimens reciprocated the seeding interval of their corresponding brace parts. For precise replication of RHS curvatures, the corner portions of RHS members were split into ten parts. Likewise, in the validation process, the corner portions of RHS members were extended by 2t into their neighbouring flat portions. For RHS members with $t \leq 6$ mm, no divisions were made along the wall thickness of the parametric FE specimens. However, for RHS members with $t > 6$ mm, the wall thickness of parametric FE specimens was divided into two layers. The use of the C3D20 element and one division along the wall thickness of FE specimens with $6 < t \leq 12.5$ provided four layers along the thickness direction. Further wall thickness divisions made the element assembly quite complex and led to unconverged results for many FE specimens investigated in this study. With regard to the weld modelling, FW was modelled for FE specimens with $\beta \leq 0.80$. However, for FE specimens with $\beta >$ 0.80, GW and FW were respectively modelled along the longitudinal and transverse directions of the chords. Following the prequalified tubular joint details given in AWS D1.1M [23], the leg size of FW was designed as 1.5 times the minimum of t_1 and t_0, which was consistent with the test program [4].

For different fire exposure series (i.e. ψ_1=300°C, ψ_2=550°C, ψ_3=750°C and ψ_4=900°C) of the FE parametric study, the corresponding measured post-fire residual static material properties of flat and corner portions of RHS 120×120×4 [10] were assigned to the flat and corner portions of the FE specimens. Figs. 8(a) and 8(b) present the measured post-fire residual static stress-strain curves of flat and corner portions of RHS 120×120×4 for different fire exposure series, respectively. Besides, the measured static weld material properties at room temperature [21] were retained as 100%, 85%, 57% and 48% for 300°C, 550°C, 750°C and 900°C post-fire temperatures, respectively. These retention percentages correspond to the average retention values of the ultimate stress of tubular members of different fire exposure series. Table 3 presents the measured post-fire residual static material properties of RHS 120×120×4 adopted in the parametric study, which include Young's modulus (E), 0.2% proof stress and strain ($\sigma_{0.2}$ and $\varepsilon_{0.2}$), ultimate stress and strain (σ_u and ε_u) and fracture strain (ε_f). Additionally, the flat parts of chord webs (i.e. h_0-2R_0) of all equal-width parametric X-joints of different fire exposure series were modelled as an outward bulging 3-point arc. The flat part of each chord web of equal-width RHS X-joint was outward bulged at its centre by 0.015b_0, as shown in Fig. 3.

3.3.3. Failure modes

Overall, the experimental [4] and numerical investigations showed three types of failure modes. First, failure of fire exposed RHS X-joint by chord flange yielding, which was termed as chord face failure and denoted by the letter 'F' in this study. Second, failure of fire exposed RHS X-joint due buckling of chord webs, which was termed as chord side wall failure and denoted by the letter 'S' in this study. Third, failure of fire exposed RHS X-joint due to the combination of chord face and chord side wall failures, which was named as combined failure and denoted by 'F+S' in this study. It is important to note that these failure modes were defined corresponding to the $N_{f,\psi}$, which in turn was computed by combinedly considering the ultimate and 0.03b_0 limit loads, whichever occurred earlier in the $N_{f,\psi}$ vs u curve. The test and parametric FE specimens were failed by the F mode, when the $N_{f,\psi}$ was determined using the 0.03b_0 limit. The applied loads of fire exposed RHS X-joints failed by the F mode were monotonically increasing. The test and parametric FE specimens were failed by the F mode in this investigation, when $0.30 \leq \beta \leq 0.75$. On the other hand, test and parametric FE specimens were failed by the S mode in this investigation, when β=1.0. For parametric FE specimens that failed by the F+S mode, the load vs deformation curves exhibited a clear ultimate load. Additionally, evident deformations of chord flange, chord webs and chord corner regions were noticed in the parametric FE specimens that failed by the F+S mode. The specimens were failed by the F+S mode in this investigation when $0.80 \leq \beta \leq 0.90$. Moreover, none of the test and FE specimens were failed by the global buckling of braces. Figs. 9 to 11 present the variations of $N_{f,\psi}$ vs u curves of typical FE X-joint specimens that failed by the F, F+S and S failure modes for all 4 post-fire temperatures, respectively.

4. Existng design provisions at ambient temperature

4.1. EC3 [6] and CIDECT [7]

Currently, design rules to predict the post-fire residual strengths of tubular joints are not given in any code and guideline. Therefore, in order to examine the suitability of EC3 [6] and CIDECT [7] design provisions for CFHSS fire exposed RHS X-joints, in this study, the nominal resistances from design equations given in EC3 [6] and CIDECT [7] ($N_{E,\psi}$ and $N_{C,\psi}$) were determined using the measured post-fire residual static material properties shown in Table 3. The existing design rules given in EC3 [6] and CIDECT [7] are shown below:

Chord face failure ($\beta \leq 0.85$)

EC3 [6]:

$$N_{E,\psi} = C_f \left[k_n \frac{f_{y0,\psi} t_0^2}{(1-\beta)\sin\theta_1} \left(\frac{2\eta}{\sin\theta_1} + 4\sqrt{1-\beta} \right) / \gamma_{M5} \right] \tag{1}$$

CIDECT [7]:

$$N_{C,\psi} = C_f \left[Q_f \frac{f_{y0,\psi} t_0^2}{\sin\theta_1} \left(\frac{2\eta}{(1-\beta)\sin\theta_1} + \frac{4}{\sqrt{1-\beta}} \right) \right] \tag{2}$$

Chord side wall failure ($\beta = 1.0$)

EC3 [6]:

$$N_{E,\psi} = C_f \left[k_n \frac{f_{b,\psi} t_0}{\sin\theta_1} \left(\frac{2h_1}{\sin\theta_1} + 10t_0 \right) / \gamma_{M5} \right] \quad (3)$$

CIDECT [7]:

$$N_{C,\psi} = C_f \left[Q_f \frac{f_{k,\psi} t_0}{\sin\theta_1} \left(\frac{2h_1}{\sin\theta_1} + 10t_0 \right) \right] \quad (4)$$

The nominal resistances from EC3 [6] were determined using 0.2% proof stress and partial safety factor (γ_{M5}) equal to 1.0. In addition, a material factor (C_f) equal to 0.80 was adopted as per EC3 [24]. On the other hand, CIDECT [7] uses the minimum of 0.2% proof stress and 0.80 times the corresponding ultimate stress for joint resistance calculation. Moreover, design provisions given in CIDECT [7] recommend the use of C_f equal to 0.90 for tubular joints with steel grade exceeding S355. Unlike EC3 [6], CIDECT [7] uses different values of partial safety factors (γ_M) for different tubular joints and their corresponding failure modes, which are given in IIW [25]. However, their effects are implicitly included inside the CIDECT [7] design provisions. As a result, nominal resistances of RHS X-joints from CIDECT [7] were calculated using γ_M equal to 1.0 and 1.25 for chord face failure and chord side wall failure, respectively. In Eqs. (1) to (4), chord stress functions are denoted by k_n and Q_f, post-fire yield stress of chord member is denoted by $f_{y0,\psi}$, the parameter η is equal to h_1/b_0, post-fire chord side wall buckling stresses are denoted by $f_{b,\psi}$ and $f_{k,\psi}$, and the angle between brace and chord is denoted by θ_1 (in degrees).

4.2. Lan et al. [8]

Lan et al. [8] proposed design rules to predict the chord sidewall failure strengths of RHS-to-RHS X-, T- and Y-joints made of steel grades up to S960. The design rules were proposed using the experimental and numerical results reported in literature, which also include different loading cases. The nominal strength of RHS-to-RHS X-joint subjected to brace axial compression loading ($N_{Lan,\psi}$) can be calculated using Eq. (5).

$$N_{Lan,\psi} = C_f f_{k,\psi} t_0 \left(2h_1 + 10t_0\right)\sqrt{\frac{1}{\sin\theta_1}} Q_f \tag{5}$$

where
$$C_f = 1.1 - \frac{0.1 f_{y0,\psi}}{355} \tag{6}$$

$$f_{k,\psi} = \left[\left(1.12 - 0.012\frac{h_0}{t_0}\sqrt{\frac{f_{y0,\psi}}{355}}\right)\left(\frac{h_0}{h_1}\right)^{0.15} f_{y0,\psi}\right] \leq f_{y0,\psi} \tag{7}$$

4.3. Kim and Lee [9]

Kim and Lee [9] studied the behaviour of RHS-to-RHS X-joints subjected to compression loading with a focus on the chord sidewall failure mode. Existing design rules given in literature for chord sidewall failure mode were analysed and the current design rule given in EC3 [6] was modified to provide design strengths for RHS-to-RHS X-joints made of steel grades up to S700 and failed by chord sidewall failure mode. The design rule proposed by Kim and Lee [9] is given as follows:

$$N_{KL,\psi} = \frac{C_f}{\gamma_M} \chi_\psi f_{y0,\psi} \left(2h_1 t_0\right) Q_f \tag{8}$$

In Eq. (8), the value of partial safety factor (γ_M) is equal to 1.12. The nominal resistance from Kim and Lee [9] ($N_{KL,\psi}$) was calculated from Eq. (8) by removing the γ_M factor. The proposed value of C_f for chord sidewall failure mode is 1.0. The term χ_ψ is the reduction factor for column buckling using the ECCS c curve and a slenderness of $(0.5\sqrt{h_1/h_0})\lambda$. The chord sidewall slenderness (λ) can be determined from EC3 [6]. In Eqs. (1) to (8), the values of k_n and Q_f were taken as 1.0.

5. Reliability analysis

In order to examine the reliability of existing and proposed design equations, a reliability study was performed as per AISI S100 [26]. Eq. (9) was used to calculate the value of reliability index (β_0). In this investigation, a lower bound value of 2.50 was defined as the target β_0. Therefore, when $\beta_0 \geq$ 2.50, the design equation was treated as reliable in this study.

$$\beta_0 = \frac{\ln(C_\phi M_m F_m P_m / \phi)}{\sqrt{V_M^2 + V_F^2 + C_P V_P^2 + V_Q^2}} \tag{9}$$

The dead load (DL)-to-live load (LL) ratio equal to 0.20 was used to compute the calibration coefficient (C_ϕ) in Eq. (9). For the material factor, the mean value and COV were respectively symbolised by M_m and V_M. For the fabrication factor, the mean value and COV were respectively symbolised by F_m and V_F. Referring to AISI S100 [26], the M_m and V_M were adopted as 1.10 and 0.10, respectively. Additionally, F_m and V_F were adopted as 1.00 and 0.10, respectively. The resistance factor required to convert nominal resistance to design resistance was denoted by ϕ. The mean value of the ratios of test and FE joint strengths-to-nominal resistances predicted from code was denoted by P_m, while the corresponding COV was denoted by V_P. The correction factor (C_P) given in AISI S100 [26] was also used in Eq. (9) to incorporate the effect of number of data under consideration. Besides, V_Q symbolised the COV of load effects. To evaluate the reliability levels of EC3 [6] design provisions, the DL and LL were combined as 1.35DL + 1.5LL [27], and thus, the calculated value of C_ϕ was 1.463. Further, to examine the reliability levels of CIDECT [7] design provisions as well as proposed design rules, the DL and LL were combined as 1.2DL + 1.6LL [28], and therefore, the calculated value of C_ϕ was 1.521.

6. Comparisons between residual joint strengths and nominal resistances

For different observed failure modes, the overall summary of comparisons between $N_{f,\psi}$ and nominal resistances predicted from design rules given in EC3 [6], CIDECT [7] and literature [8,9] are shown in Tables 4 to 6. In total, 765 data are presented in Tables 4 to 6, including 9 test data [4] and 756 parametric FE data generated in this study. The comparisons are also graphically shown in Figs. 12 to 15 for different failure modes. Table 4 and Fig. 12 present the comparisons for test and parametric FE specimens that failed by the F mode. The comparison results proved that the design rules given in EC3 [6] and CIDECT [7] are slightly conservative but very scattered and unreliable for the design of CFHSS fire exposed RHS X-joints.

In Fig. 12, generally, test and parametric FE specimens with small values of β and η ratios and large values of 2γ ratio lie below the unit slope line (i.e. y=x). For such specimens, the joint resistance corresponding to the $0.03b_0$ limit was not sufficient to cause the yielding of chord flanges. On the contrary, the yield line theory was used to derive the existing design equation for RHS X-joint specimens that failed by the F mode [6,7]. Consequently, $N_{f,\psi}$ of test and parametric FE specimens became smaller than the corresponding nominal resistances predicted from design rules given in EC3 [6] and CIDECT [7]. As a result, such cases fall below the line of unit slope. The data above the line of unit slope, on the other hand, indicate test and parametric FE specimens with medium to large values of β and η ratios and small values of 2γ ratio. The stress-strain behaviour of HSS material is quite different to that of mild steel [29-33], which could change the deformation extent of chord connecting faces.

The comparison results of fire exposed RHS X-joints that failed by the F+S mode are shown in Table 5 and Fig. 13. The comparison results proved that using post-fire yield strengths the current design provisions given in EC3 [6] and CIDECT [7] have demonstrated to be quite conservative but unreliable. The data above the unit slope line in Fig. 13 typically represent RHS X-joints with large values of β ratio and small values of 2γ and h_0/t_0 ratios. As the β ratio of RHS X-joint failed by the F+S mode increased, the brace member gradually approached the chord corner regions. Consequently, $N_{f,\psi}$ of such joints increased due to the enhanced rigidity of chord corner regions. On the other hand, the corresponding increase in nominal resistances predicted from design rules given in EC3 [6] and CIDECT [7] was lower than the $N_{f,\psi}$ of RHS X-joints. Subsequently, such data fall above the line of unit slope in Fig. 13.

Table 6 and Figs. 14 and 15 present the comparison results of the test and parametric FE specimens that failed by the S mode. The current design rules given in EC3 [6] and CIDECT [7] apparently provided very conservative predictions and were accompanied by significantly large values of COV. It is due to the assumption of chord webs as pin-ended columns, which resulted in very conservative predictions as h_0/t_0 ratio increased. The predictions from design rule proposed by Lan et al. [8] are quite conservative but highly scattered and unreliable for the range of fire exposed RHS X-joints investigated in this study. On the other hand, design rule proposed by Kim and Lee [9] demonstrated to be moderately conservative and reliable for the proposed resistance factor (1/1.12).

7. Proposed design rules

Using two design methods, named as proposal-1 and -2, design rules are proposed in this study for different failure modes of the investigated fire exposed RHS X-joints. The design rules proposed in both the methods (i.e. proposal-1 and -2) were based on design equations proposed by Pandey and Young [34] for without fire exposed S960 steel grade RHS X-joints. In the first design method (i.e. proposal-1), the room temperature material properties used in the design equations proposed by Pandey and Young [34] are replaced with the corresponding post-fire residual material properties. In addition, a correction factor (ξ) based on post-fire peak temperature (ψ) is also applied on the proposed design rules. On the other hand, in the second design method (i.e. proposal-2), only a correction factor based on the post-fire peak temperature (ψ) is applied on the design rules proposed by Pandey and Young [34] using the room temperature material properties. Therefore, design equations under proposal-1 can predict the $N_{f,\psi}$ of fire exposed RHS X-joints when post-fire residual material properties are available. However, design equations under proposal-2 can predict the $N_{f,\psi}$ only using the post-fire peak temperature (ψ). It should be noted that the design rules proposed in this study are valid for 300°C $\leq \psi \leq$ 900°C. In this study, the validity ranges of important factors influencing the static behaviour of RHS X-joints were extended beyond their existing limits given in EC3 [6] and CIDECT [7]. Furthermore, as welds were modelled in all parametric FE specimens, the influence of weld was implicitly included in the proposed design rules. In order to obtain design resistances (N_d), the proposed nominal resistances (N_{pn1} and N_{pn2}) in the following sub-sections of this paper shall be multiplied by their correspondingly recommended resistance factors (ϕ), i.e. $N_d = \phi\ (N_{pn1}$ or $N_{pn2})$.

7.1. Chord face failure (F) mode ($0.30 \leq \beta \leq 0.75$)

The design equations proposed under proposal-1 and -2 for fire exposed RHS X-joints failed by the

F mode are as follows:

Proposal-1:

Using post-fire material properties and post-fire peak temperature (ψ) correction factor:

$$N_{pn1} = \xi\left[f_{y0,\psi}t_0^2\left(\frac{28\beta+7\eta-7}{1+0.01(2\gamma)}\right)\right] \tag{10}$$

where

$$\xi = \begin{cases} 0.0002\psi + 0.85 & \text{for} \quad 300°\text{C} \le \psi \le 750°\text{C} \\ 0.0024\psi - 0.80 & \text{for} \quad 750°\text{C} < \psi \le 900°\text{C} \end{cases} \tag{11}$$

Proposal-2:

Using room temperature material properties and post-fire peak temperature (ψ) correction factor:

$$N_{pn2} = (1.2 - 0.0008\psi)\left[f_{y0}t_0^2\left(\frac{28\beta+7\eta-7}{1+0.01(2\gamma)}\right)\right] \tag{12}$$

The Eqs. (10) and (12) are valid for $0.30 \le \beta \le 0.75$, $16.6 \le 2\gamma \le 50$, $16.6 \le h_0/t_0 \le 50$, $0.3 \le \eta \le 1.2$ and $0.75 \le \tau \le 1.0$. As shown in Table 4, the P_m and V_p of proposal-1 (i.e. Eq. (10)) are 1.00 and 0.147, respectively, while the P_m and V_p of proposal-2 (i.e. Eq. (12)) are 1.01 and 0.148, respectively. For both Eqs. (10) and (12), ϕ equal to 0.80 is recommended, resulting in β_0 equal to 2.51 and 2.54, respectively. Thus, both Eqs. (10) and (12) must be multiplied by ϕ equal to 0.80 to obtain their corresponding design resistances (N_d). The comparisons of $N_{f,\psi}$ of test and FE specimens with nominal resistances predicted from design equations given in EC3 [6], CIDECT [7] as well as predictions from proposal-1 and -2 are graphically presented in Fig. 12. Compared to the design provisions given in EC3 [6] and CIDECT [7], the Eqs. (10) and (12) are relatively more accurate, less scattered and reliable.

7.2. Combined failure (F+S) mode ($0.80 \le \beta \le 0.90$)

The design equations proposed under proposal-1 and -2 for fire exposed RHS X-joints failed by the

F+S mode are as follows:

Proposal-1:

Using post-fire material properties and post-fire peak temperature (ψ) correction factor:

$$N_{pn1} = \xi\left[f_{y0,\psi}t_0^2\left(\frac{60\beta+8\eta-38}{0.9+0.003(2\gamma)}\right)\right] \tag{13}$$

where

$$\xi = \begin{bmatrix} 0.9 & \text{for} \quad 300°\text{C} \le \psi \le 750°\text{C} \\ 0.0027\psi - 1.13 & \text{for} \quad 750°\text{C} < \psi \le 900°\text{C} \end{bmatrix} \tag{14}$$

Proposal-2:

Using room temperature material properties and post-fire peak temperature (ψ) correction factor:

$$N_{pn2} = (1.17 - 0.0008\psi)\left[f_{y0}t_0^2\left(\frac{60\beta+8\eta-38}{0.9+0.003(2\gamma)}\right)\right] \tag{15}$$

The Eqs. (13) and (15) are valid for $0.80 \le \beta \le 0.90$, $16.6 \le 2\gamma \le 50$, $16.6 \le h_0/t_0 \le 50$, $0.6 \le \eta \le 1.2$ and $0.75 \le \tau \le 1.0$. As shown in Table 5, the P_m and V_p of proposal-1 (i.e. Eq. (13)) are 1.03 and 0.167, respectively, while the P_m and V_p of proposal-2 (i.e. Eq. (15)) are 1.03 and 0.169, respectively. For both Eqs. (13) and (15), ϕ equal to 0.80 is recommended, which resulted in β_0 equal to 2.52 and 2.50, respectively. Thus, both Eqs. (13) and (15) must be multiplied by ϕ equal to 0.80 to obtain their corresponding design resistances (N_d). The comparisons of $N_{f,\psi}$ of RHS X-joints with nominal resistances predicted from design equations given in EC3 [6], CIDECT [7] as well as predictions from proposal-1 and -2 are graphically presented in Fig. 13. Compared to the design provisions given in EC3 [6] and CIDECT [7], the Eqs. (13) and (15) are relatively more accurate, less scattered and reliable.

7.3. Chord side wall failure (S) mode (β = 1.0)

The design equations proposed under proposal-1 and -2 for fire exposed RHS X-joints failed by the

S mode are as follows:

<u>Proposal-1:</u>

Using post-fire material properties and post-fire peak temperature (ψ) correction factor:

$$N_{pn1} = (1.04 - 0.0004\psi)\left[\frac{f_{k,\psi}(2b_w t_0)}{(0.4\eta + 2)}\left(\frac{1.4 - 0.05(2\gamma) + 2.4\tau}{2e^{-0.05\left(\frac{h_0}{t_0}\right)}}\right)\right] \tag{16}$$

<u>Proposal-2:</u>

Using room temperature material properties and post-fire peak temperature (ψ) correction factor:

$$N_{pn2} = (1.34 - 0.001\psi)\left[\frac{f_k(2b_w t_0)}{(0.4\eta + 2)}\left(\frac{1.4 - 0.05(2\gamma) + 2.4\tau}{2e^{-0.05\left(\frac{h_0}{t_0}\right)}}\right)\right] \tag{17}$$

The Eqs. (16) and (17) are valid for $\beta = 1.0$, $16.6 \leq 2\gamma \leq 50$, $10 \leq h_0/t_0 \leq 60$, $0.6 \leq \eta \leq 1.2$ and $0.75 \leq \tau \leq 1.25$. As shown in Table 6, the P_m and V_p of proposal-1 (i.e. Eq. (16)) are 1.04 and 0.179, respectively, while the P_m and V_p of proposal-2 (i.e. Eq. (17)) are 1.06 and 0.186, respectively. For both Eqs. (16) and (17), ϕ equal to 0.80 is recommended, which resulted in β_0 equal to 2.51 and 2.54, respectively. Thus, both Eqs. (16) and (17) must be multiplied by ϕ equal to 0.80 to obtain their corresponding design resistances (N_d). The comparisons of $N_{f,\psi}$ of test and FE specimens with nominal resistances predicted from design equations given in EC3 [6], CIDECT [7] as well as predictions from proposal-1 and -2 are graphically presented in Fig. 14. On the other hand, Fig. 15 presents the comparisons of $N_{f,\psi}$ of test and FE specimens with nominal resistances predicted from design equations given in Lan et al. [8] and Kim and Lee [9] as well as predictions from proposal-1 and -2. Compared to the design provisions given in EC3 [6], CIDECT [7], Lan et al. [8] and Kim and Lee [9], the Eqs. (16) and (17) are relatively more accurate, less scattered and reliable. The buckling curve 'a' of EC3 [35] was used to determine the $f_{k,\psi}$ and f_k in Eqs. (16) and (17). Moreover, the flat portions of chord side walls were equal to h_0-$2R_0$. Additionally, instead of assuming pin-ended boundary conditions for the flat portions of chord side walls, the effective length of chord side wall column was determined using a factor equal to 0.85. Therefore, in this study, the effective lengths of the flat portions of chord side walls were equal to $0.85\times(h_0\text{-}2R_0)$. The definition of the width of chord web column (b_w) was identical to that given in EC3 [6] and CIDECT [7].

It is important to note that for RHS X-joint specimens with $0.75 < \beta < 0.80$ and $0.90 < \beta < 1.0$, the nominal resistances under proposal-1 can be obtained by performing linear interpolation between Eqs. (10) and (13) as well as Eqs. (13) and (16), respectively. Similarly, under proposal-2, the nominal resistances of RHS X-joint specimens with $0.75 < \beta < 0.80$ and $0.90 < \beta < 1.0$ can be obtained by performing linear interpolation between Eqs. (12) and (15) as well as Eqs. (15) and (17), respectively.

8. Conclusions

The post-fire static behaviour of cold-formed S960 steel grade RHS X-joints subjected to axial compression loads is numerically investigated in this study. The residual static strengths of RHS X-joints were investigated corresponding to 300°C, 550°C, 750°C and 900°C post-fire temperatures. In order to perform numerical investigation, the measured post-fire residual static material properties corresponding to 300°C, 550°C, 750°C and 900°C post-fire temperatures of S960 steel grade RHS members [10] were used. An accurate finite element (FE) model was developed using the test results reported in Pandey and Young [4]. Using the validated FE model, an extensive numerical parametric study comprising of 756 FE specimens was performed. The inclusion of welds in all FE models appreciably improved the accuracies of numerical results. Overall, RHS X-joints were failed by three failure modes, including chord face failure (F), chord side wall failure (S), and a combination of these two failure modes, i.e. combined failure (F+S) mode. The nominal resistances predicted from design rules given in EC3 [6], CIDECT [7], Lan et al. [8] and Kim and Lee [9], using post-fire residual material properties, were compared with the residual strengths of RHS X-joints investigated in this study. Generally, it has been demonstrated that the design rules given in EC3 [6] and CIDECT [7] as well as the literature [8,9] are quite conservative but scattered for the range of fire exposed RHS X-joints investigated in this study with extended validity limits of governing geometric parameters. Therefore, accurate, less scattered and reliable design rules are proposed in this study for the design of S960 steel grade RHS X-joints. The proposed design rules are valid for post-fire temperatures ranging from 300°C to 900°C.

Acknowledgement

The work described in this paper was fully supported by a grant from the Research Grants Council of the Hong Kong Special Administrative Region, China (Project No. 17210218).

References

[1] Jin M, Zhao J, Chang J and Zhang D. Experimental and parametric study on the post-fire behavior of tubular T-joint. Journal of Constructional Steel Research, 70, 93-100. 2012.

[2] Gao F, Gua, XQ, Zhu HP and Xia Y. Hysteretic behaviour of tubular T-joints reinforced with doubler plates after fire exposure. Thin-Walled Structures, 92, 10-20, 2015.

[3] Gao F, Zhu H, Liang H and Tian Y. Post-fire residual strength of steel tubular T-joint with concrete-filled chord. Journal of Constructional Steel Research, 139, 327-338, 2017.

[4] Pandey M and Young B. Post-Fire Behaviour of Cold-Formed High Strength Steel Tubular T- and X-Joints, Journal of Constructional Steel Research 2021;186:106859.

[5] ISO-834. Fire-resistance tests-Elements of Building Construction-Part 1-General requirements. ISO 834-1, International Organization of Standards, 1999.

[6] Eurocode 3 (EC3), Design of Steel Structures-Part 1-8: Design of Joints, EN 1993-1-8, European Committee for Standardization, CEN, Brussels, Belgium, 2005.

[7] Packer JA, Wardenier J, Zhao XL, Vegte GJ van der, Kurobane Y. Design guide for rectangular hollow section (RHS) joints under predominantly static loading. Comite´ International pour le Developpement et l'Etude de la Construction TuECbulaire (CIDECT), Design Guide No. 3, 2nd edn., LSS Verlag, Dortmund, Germany, 2009.

[8] Lan X, Wardenier J and Packer JA. Design of chord sidewall failure in RHS joints using steel grades up to S960. Thin-Walled Structures, 2021;163:107605.

[9] Kim SH and Lee CH. Chord sidewall failure of RHS X-Joints in compression and associated design recommendations. Journal of Structural Engineering, 2021; 147(8):04021111.

[10] Pandey M and Young B. Post-fire Mechanical Response of High Strength Steels. Thin-Walled Structures, 164 (2021) 107606.

[11] Abaqus/Standard. Version 6.17. USA: K. a. S. Hibbit; 2017.

[12] Pandey M, Chung KF and Young B. Design of cold-formed high strength steel tubular T-joints under compression loads. Thin-Walled Structures 2021;164:107573.

[13] Pandey M, Chung KF and Young B. Numerical investigation and design of fully chord supported tubular T-joints. Engineering Structures 2021;239:112063.

[14] Crockett P. Finite element analysis of welded tubular connections. PhD Thesis, University of Nottingham, 1994.

[15] Ma JL, Chan TM and Young B. Design of cold-formed high strength steel tubular beams. Engineering Structures 2017; 151:432-443.

[16] Li QY and Young B. Design of cold-formed steel built-up open section members under combined compression and bending. Thin-Walled Structures. 2022;172:108890.

[17] Li HT and Young B. Cold-formed stainless steel RHS members undergoing combined bending and web crippling: Testing, modelling and design. Engineering Structures 2022;250:113466.

[18] Garifullin M, Bronzova MK, Heinisuo M, Mela K and Pajunen S. Cold-formed RHS T joints with initial geometrical imperfections. Magazine of Civil Engineering 2018,82(6).

[19] prEN 10219-2. Cold formed welded structural hollow sections of non-alloy and fine grain steels-Part 2: Tolerances, dimensions and sectional properties. European Committee for Standardization (CEN), Brussels, Belgium; 2006.

[20] Pandey M and Young B. Tests of cold-formed high strength steel tubular T-joints. Thin-Walled Struct 2019;143:106200.

[21] Pandey M and Young B. Compression capacities of cold-formed high strength steel tubular T-joints. J Constr Steel Res 2019;162:105650.

[22] SSAB. Strenx Tube 960 MH. Data Sheet 2043, Sweden, 2017.

[23] AWS D1.1/D1.1M, Structural Welding Code – Steel, American Welding Society (AWS),

Miami, USA, 2020.
[24] Eurocode 3 (EC3), Design of steel structures. Part 1-12: Additional rules for the extension of EN 1993 up to steel grades S700, EN 1993-1-12, European Committee for Standardization, CEN, Brussels, Belgium, 2007.
[25] IIW Doc. XV-1402-12 and IIW Doc. XV-E-12-433. Static design procedure for welded hollow section joints – Recommendations. International Institute of Welding, Paris, France, 2012.
[26] AISI S100. North American Specification for the design of cold-formed steel structural members. American Iron and Steel Institute (AISI), Washington, D.C., USA, 2016.
[27] EN 1990. Eurocode: Basis of structural design. European Committee for Standardization (CEN), Brussels, Belgium, 2002.
[28] ASCE/SEI 7. Minimum Design Loads for Buildings and Other Structures. American Society of Civil Engineers (ASCE), New York, USA, 2016.
[29] Pandey M and Young B. Structural performance of cold-formed high strength steel tubular X-Joints under brace axial compression. Engineering Structures, 2020; 208:109768.
[30] Pandey M and Young B. Ultimate Resistances of Member-Rotated Cold-Formed High Strength Steel Tubular T-Joints under Compression Loads, Engineering Structures 2021;244:112601.
[31] Pandey M and Young B. Effect of Member Orientation on the Static Strengths of Cold-Formed High Strength Steel Tubular X-Joints, Thin-walled Structures 2022;170:108501.
[32] Pandey M and Young B. Stress Concentration Factors of Cold-Formed High Strength Steel Tubular T-Joints, Thin-walled Structures 2021;166:107996.
[33] Pandey M and Young B. Experimental Investigation on Stress Concentration Factors of Cold-formed High Strength Steel Tubular X-Joints, Engineering Structures 2021;243:112408.
[34] Pandey M and Young B. Static Performance and Design of Cold-formed High Strength Steel Rectangular Hollow Section X-Joints, Engineering Structures (in press).
[35] Eurocode 3 (EC3), Design of Steel Structures–Part 1-1: General Rules and Rules for Buildings, EN 1993-1-1, European Committee for Standardization (CEN), Brussels, Belgium, 2005.

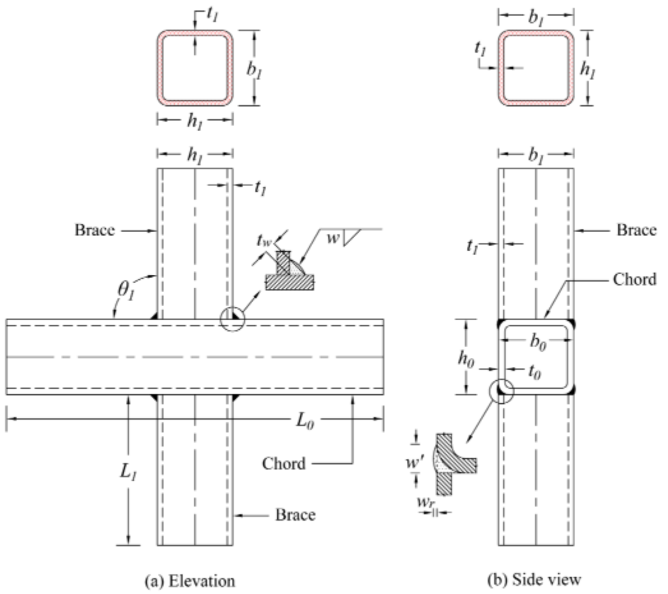

Fig. 1. Definitions of notations for RHS X-joint.

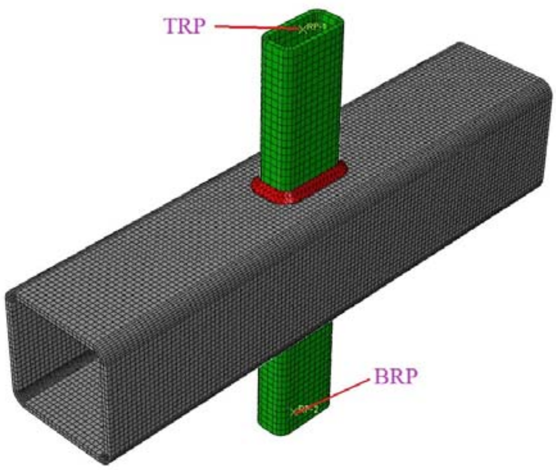

(a) Typical RHS X-joint FE model with β=0.30.

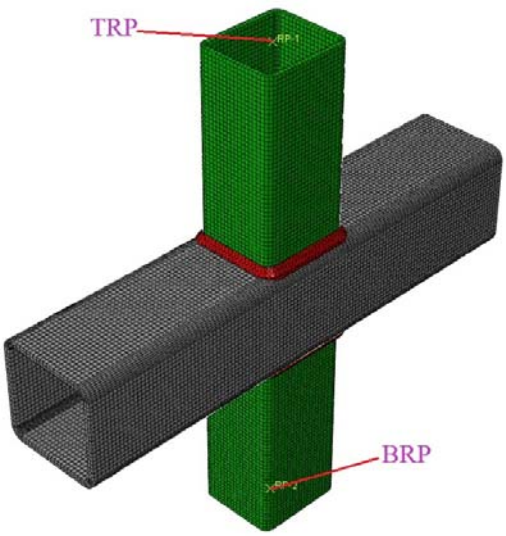

(b) Typical RHS X-joint FE model with β=0.80.

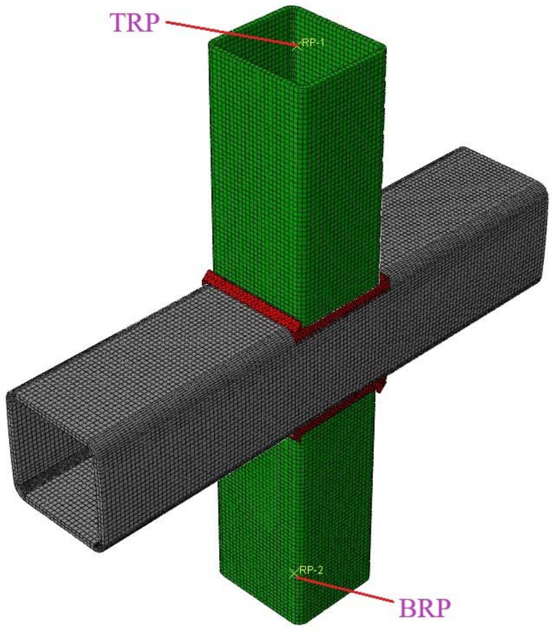

(c) Typical RHS X-joint FE model with β=1.0.

Fig. 2. Typical FE models of RHS X-joints.

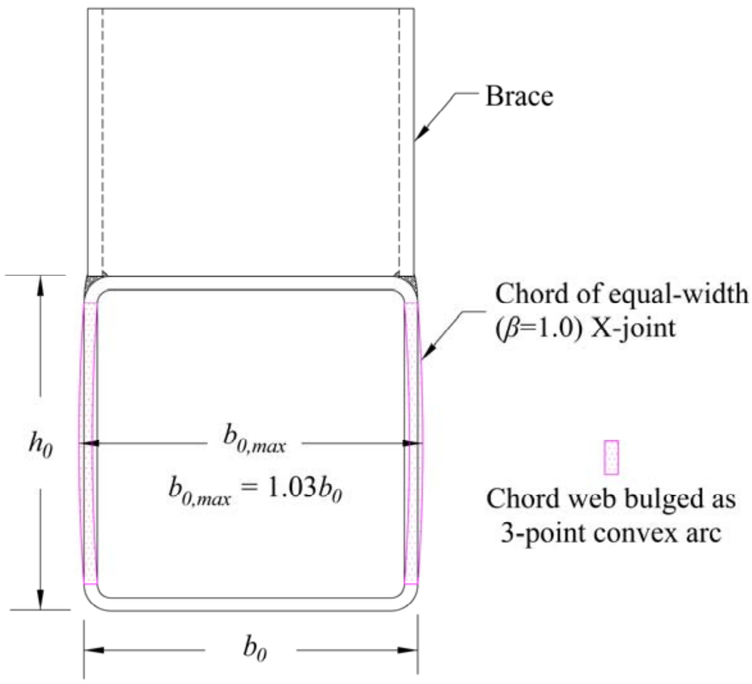

Fig. 3. Modelling of initial imperfection in chord webs of equal-width (β=1.0) RHS X-joints.

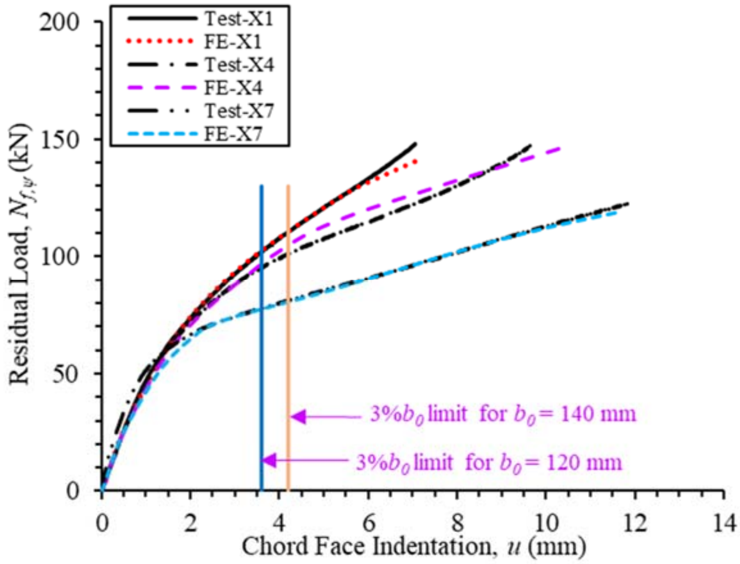

(a) Residual Load vs chord face indentation curves.

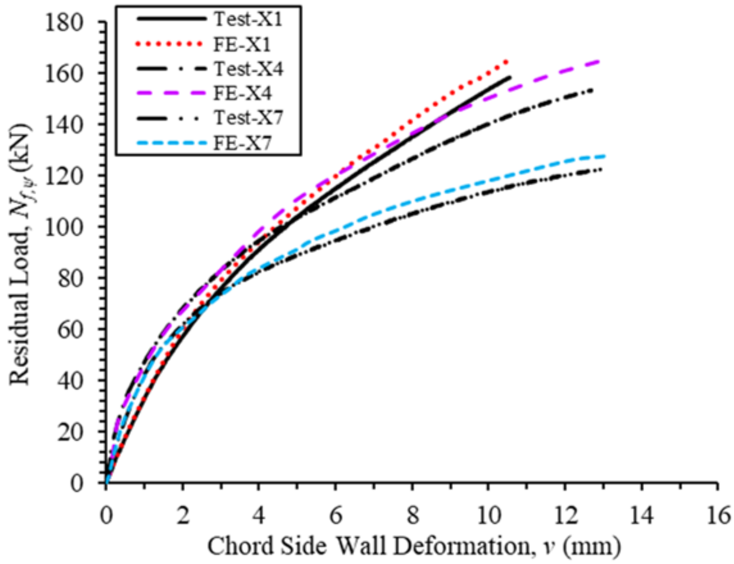

(b) Residual Load vs chord side wall deformation curves.

Fig. 4. Test vs FE load-deformation curves for RHS X-joints failed by F mode.

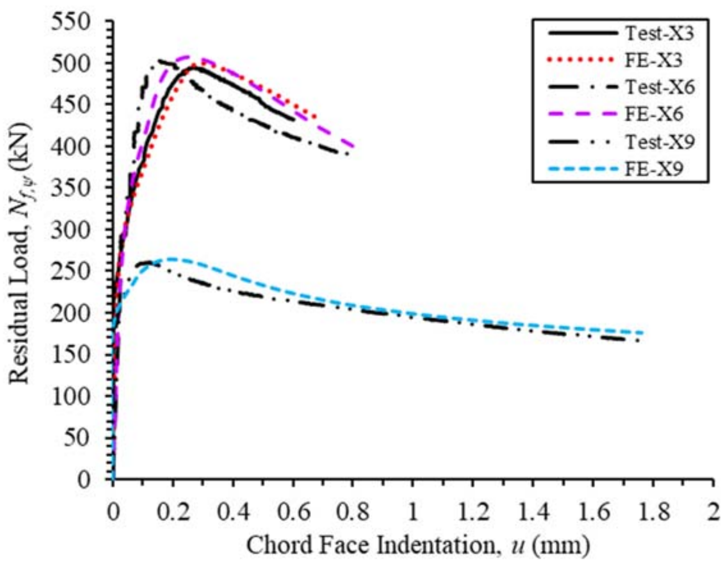

(a) Residual Load vs chord face indentation curves.

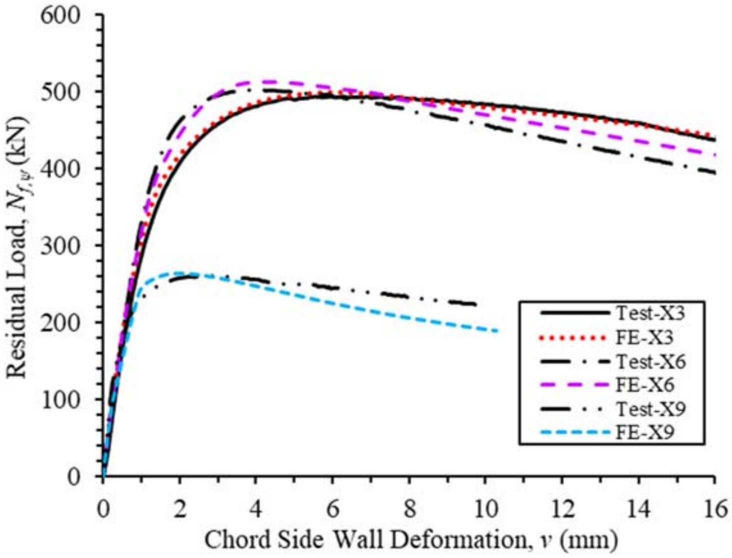

(b) Residual Load vs chord side wall deformation curves.

Fig. 5. Test vs FE load-deformation curves for RHS X-joints failed by S mode.

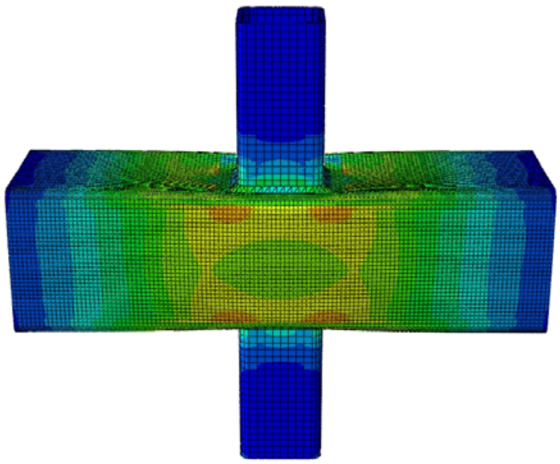

(a) Test vs FE comparison for RHS X-joint (X2) with ψ = 300°C and failed by F mode.

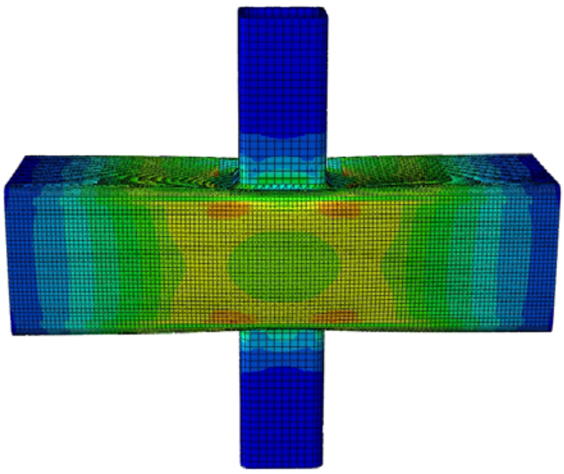

(b) Test vs FE comparison for RHS X-joint (X5) with ψ = 550°C and failed by F mode.

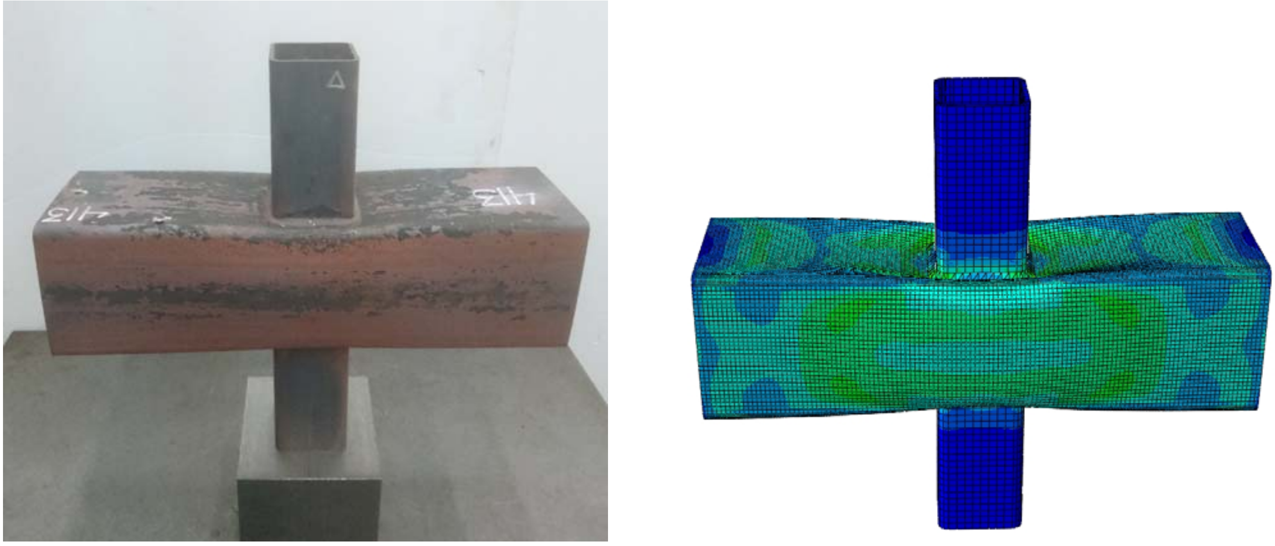

(c) Test vs FE comparison for RHS X-joint (X8) with ψ = 750°C and failed by F mode.

Fig. 6. Test vs FE comparison for RHS X-joints failed by F mode.

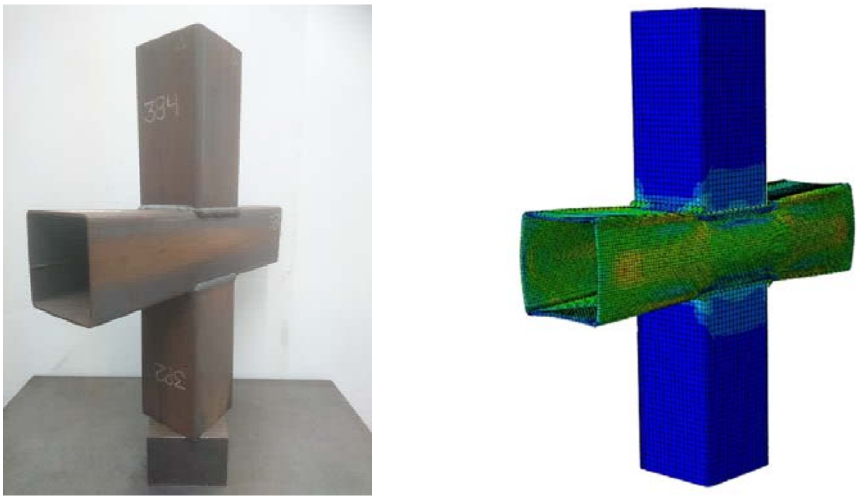

(a) Test vs FE comparison for RHS X-joint (X3) with ψ = 300°C and failed by S mode.

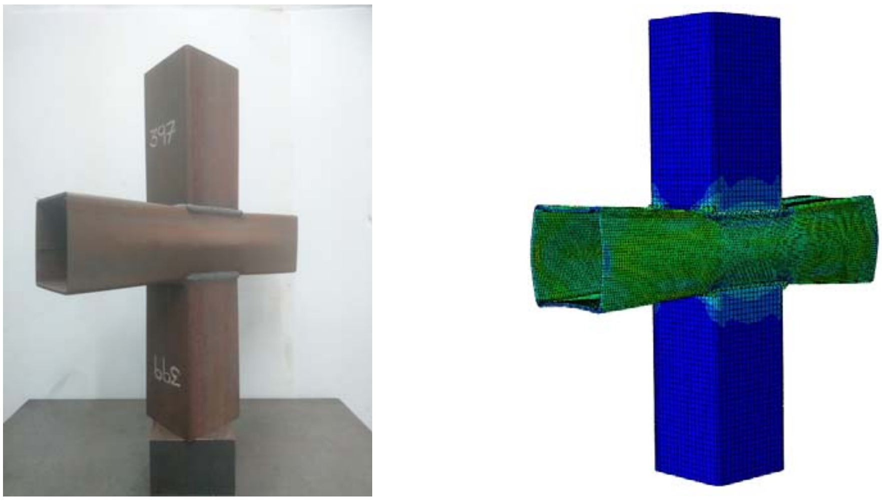

(b) Test vs FE comparison for RHS X-joint (X6) with ψ = 550°C and failed by S mode.

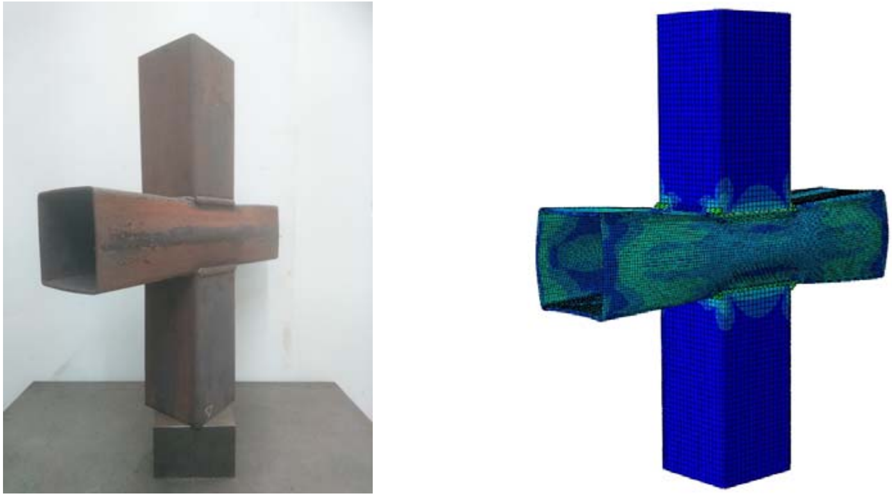

(c) Test vs FE comparison for RHS X-joint (X9) with ψ = 750°C and failed by S mode.

Fig. 7. Test vs FE comparison for RHS X-joints failed by S mode.

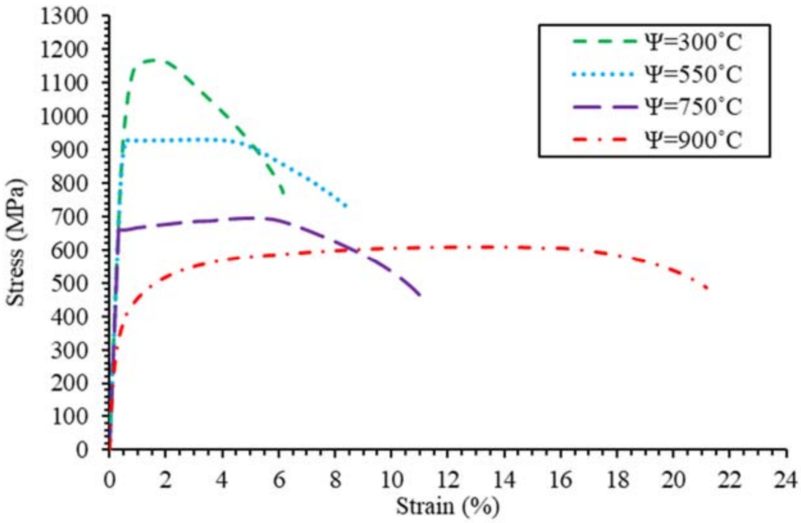

(a) For flat portion.

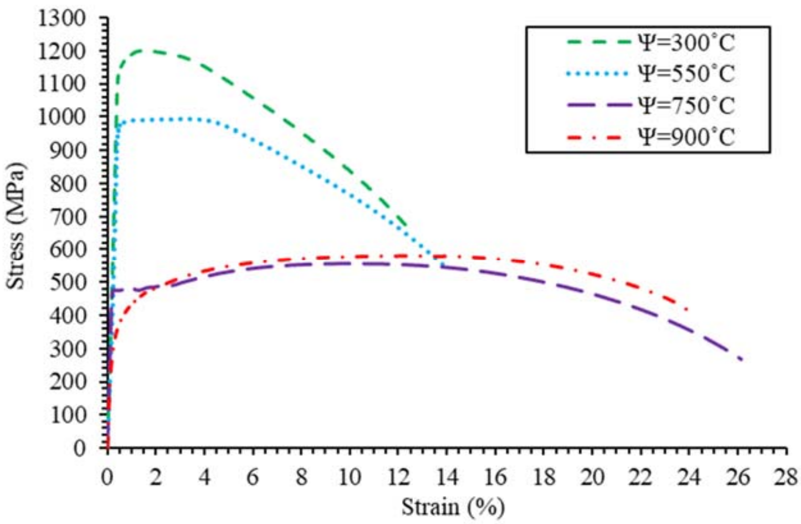

(b) For corner portion.

Fig. 8. Measured static post-fire stress-strain curves of RHS 120×120×4 [10].

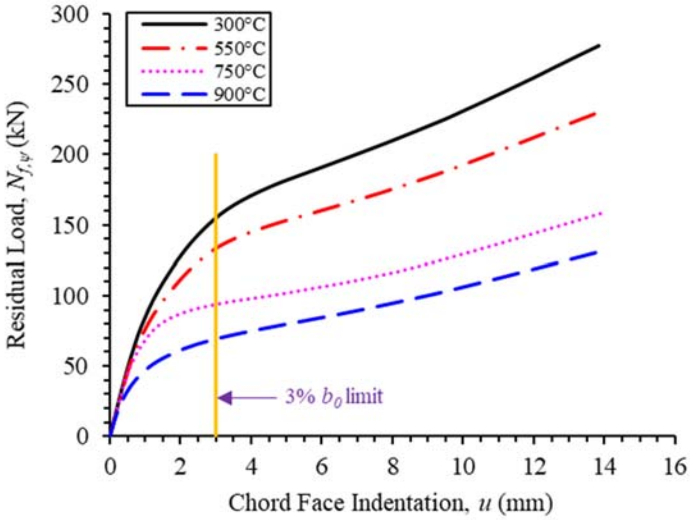

Fig. 9. Variations of load vs deformation curves for typical RHS X-joint (X-30×30×4.5-100×100×6; β=0.30) failed by F mode for different fire exposures.

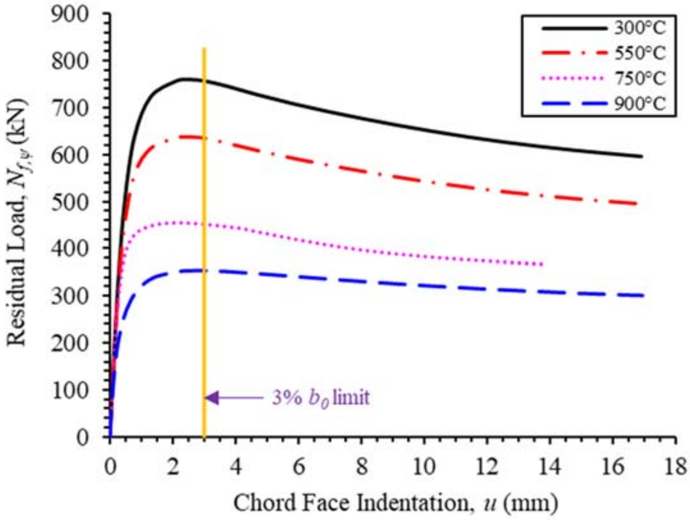

Fig. 10. Variations of load vs deformation curves for typical RHS X-joint (X-80×120×4.5-100×100×6; β=0.80) failed by F+S mode for different fire exposures.

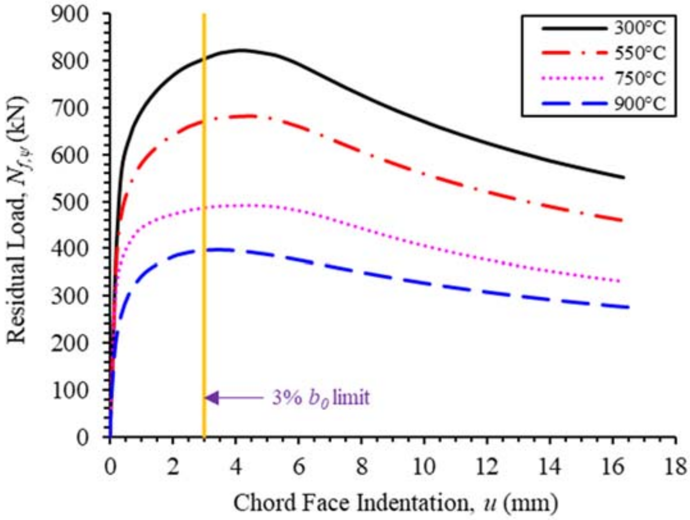

Fig. 11. Variations of load vs deformation curves for typical RHS X-joint (X-100×60×4.5-100×100×6; β=1.0) failed by S mode for different fire exposures.

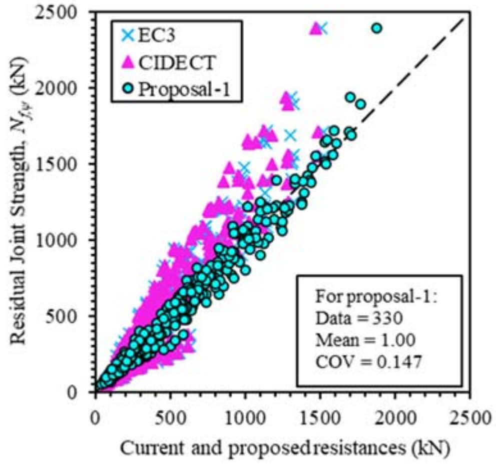

(a) For Proposal-1.

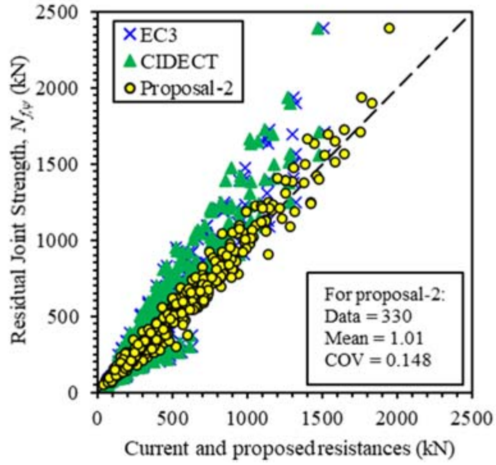

(b) For Proposal-2.

Fig. 12. Comparisons of residual joint strengths with current and proposed nominal resistances for RHS X-joints failed by F mode.

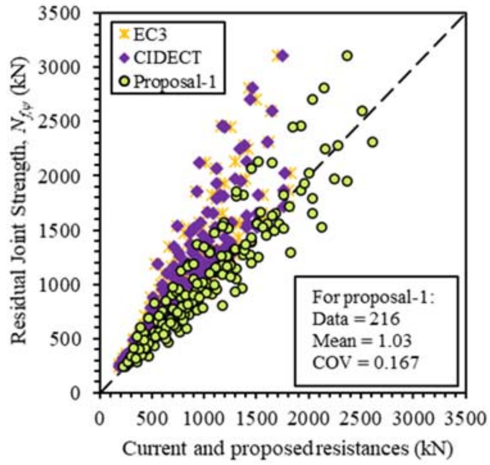

(a) For Proposal-1.

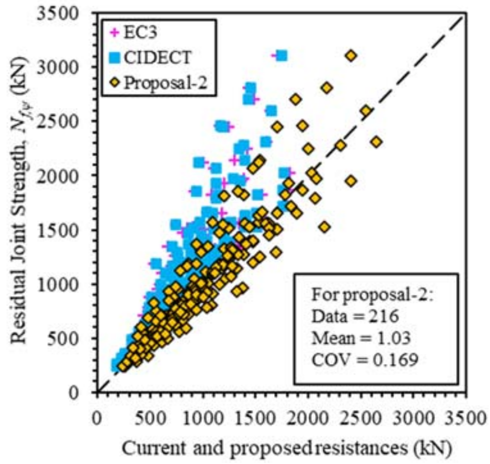

(b) For Proposal-2.

Fig. 13. Comparisons of residual joint strengths with current and proposed nominal resistances for RHS X-joints failed by F+S mode.

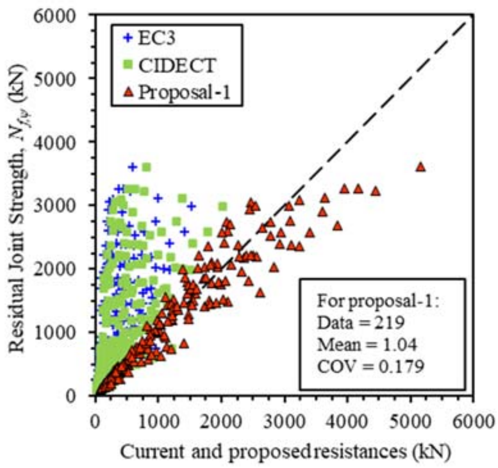

(a) For Proposal-1.

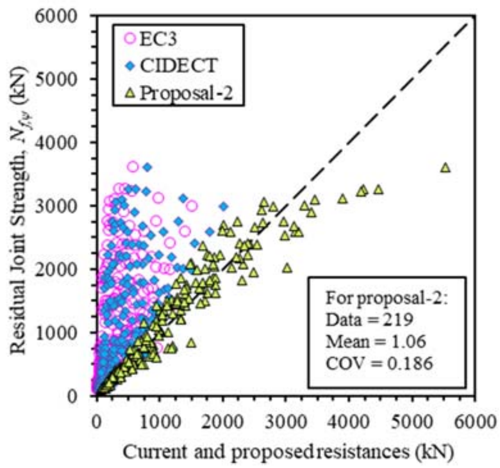

(b) For Proposal-2.

Fig. 14. Comparisons of residual joint strengths with current and proposed nominal resistances for RHS X-joints failed by S mode.

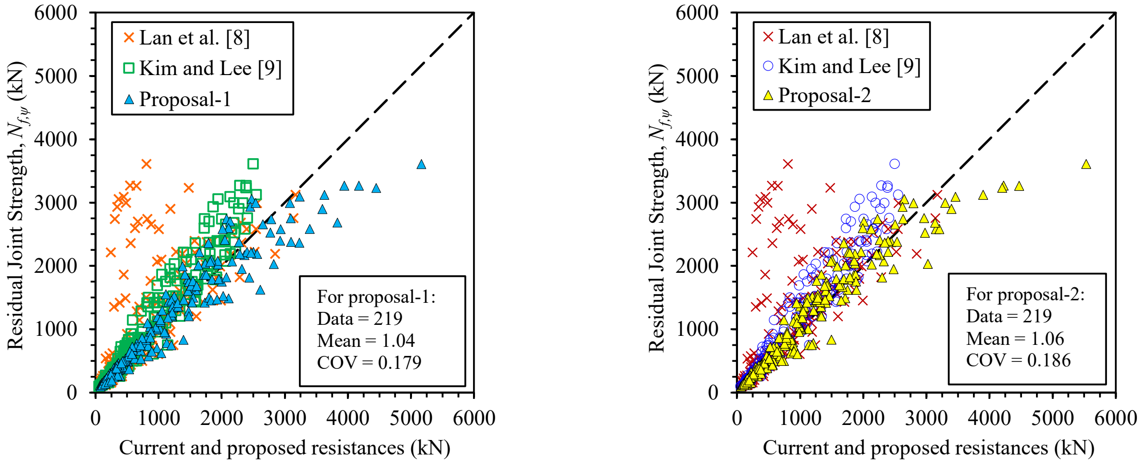

(a) For Proposal-1.

(b) For Proposal-2.

Fig. 15. Comparisons of residual joint strengths with nominal resistances predicted from Lan et al. [8], Kim and Lee [9] and proposed nominal resistances for RHS X-joints failed by S mode.

Table 1. Test vs FE residual strength comparisons for fire exposed RHS X-joints.

Specimen numbers	Specimens $X\text{-}b_1{\times}h_1{\times}t_1\text{-}b_0{\times}h_0{\times}t_0\text{-}\Psi$	β	Test Strengths[#] (kN) $N_{f,\Psi}$	FE Strengths (kN) N_{FE}	$\frac{N_{f,\psi}}{N_{FE}}$
X1	X-50×100×4-120×120×4-P300°C	0.42	102.9	103.0	1.00
X2	X-80×80×4-140×140×4-P300°C	0.57	120.3	120.4	1.00
X3	X-140×140×4-140×140×4-P300°C	1.00	495.0	499.5	0.99
X4	X-50×100×4-120×120×4-P550°C	0.41	95.3	96.0	0.99
X5	X-80×80×4-140×140×4-P550°C	0.57	107.9	108.2	1.00
X6	X-140×140×4-140×140×4-P550°C	1.00	502.7	507.1	0.99
X7	X-50×100×4-120×120×4-P750°C	0.41	77.9	77.5	1.01
X8	X-80×80×4-140×140×4-P750°C	0.57	65.3	65.1	1.00
X9	X-140×140×4-140×140×4-P750°C	1.00	260.6	264.2	0.99
				Mean (P_m)	1.00
				COV (V_p)	0.006

Note: [#]Data obtained from Pandey and Young [4].

Table 2. Overall ranges of critical parameters used in parametric study.

Parameters	Validity Ranges
ψ	[300°C to 900°C]
β (b_1/b_0)	[0.30 to 1.0]
2γ (b_0/t_0)	[16.6 to 50]
h_0/t_0	[10 to 60]
η (h_1/b_0)	[0.3 to 1.2]
τ (t_1/t_0)	[0.75 to 1.25]

Table 3. Post-fire material properties of tubular members used in parametric study [10].

Post-fire Temperatures (ψ)	Tubular Members	Regions	Measured Post-fire Material Properties E (GPa)	$\sigma_{0.2}$ (MPa)	$\varepsilon_{0.2}$ (%)	σ_u (MPa)	$0.80\sigma_u$ (MPa)	ε_u (%)	ε_f (%)
300°C	RHS (120×120×4)	Flat	222	1078	0.69	1167	934	1.60	6.16*
	RHS (120×120×4)	Corner	237	1168	0.69	1200	960	1.54	12.43#
550°C	RHS (120×120×4)	Flat	216	928	0.63	930	744	3.31	8.43*
	RHS (120×120×4)	Corner	198	983	0.70	993	794	3.39	13.99#
750°C	RHS (120×120×4)	Flat	209	660	0.52	695	556	5.18	11.22*
	RHS (120×120×4)	Corner	239	476	0.40	556	445	9.91	26.14#
900°C	RHS (120×120×4)	Flat	201	347	0.37	609	487	13.51	21.17*
	RHS (120×120×4)	Corner	203	348	0.37	580	464	12.32	23.90#

Note: *fracture strain based on 50 mm gauge length; #fracture strain based on 25 mm gauge length.

Table 4. Summary of comparisons between test and FE residual strengths with existing and proposed nominal resistances for RHS X-joints failed by F mode.

Post-fire Temperatures (ψ)	Parameters	Comparisons			
		$\frac{N_{f,\psi}}{N_{E,\psi}}$	$\frac{N_{f,\psi}}{N_{C,\psi}}$	$\frac{N_{f,\psi}}{N_{pn1}}$	$\frac{N_{f,\psi}}{N_{pn2}}$
300°C	No. of data (n)	83	83	83	83
	Mean (P_m)	1.07	1.10	1.02	0.99
	COV (V_p)	0.300	0.300	0.158	0.156
550°C	No. of data (n)	83	83	83	83
	Mean (P_m)	1.07	1.18	0.96	1.07
	COV (V_p)	0.282	0.282	0.139	0.137
750°C	No. of data (n)	83	83	83	83
	Mean (P_m)	1.11	1.17	0.98	1.02
	COV (V_p)	0.244	0.244	0.140	0.139
900°C	No. of data (n)	81	81	81	81
	Mean (P_m)	1.28	1.28	1.03	0.96
	COV (V_p)	0.270	0.270	0.139	0.139
Overall	No. of data (n)	330	330	330	330
	Mean (P_m)	1.13	1.18	1.00	1.01
	COV (V_p)	0.284	0.279	0.147	0.148
	Resistance factor (ϕ)	1.00	1.00	0.80	0.80
	Reliability index (β_0)	1.57	1.81	2.51	2.54

Table 5. Summary of comparisons between test and FE residual strengths with existing and proposed nominal resistances for RHS X-joints failed by F+S mode.

Post-fire Temperatures (ψ)	Parameters	Comparisons			
		$\frac{N_{f,\psi}}{N_{E,\psi}}$	$\frac{N_{f,\psi}}{N_{C,\psi}}$	$\frac{N_{f,\psi}}{N_{pn1}}$	$\frac{N_{f,\psi}}{N_{pn2}}$
300°C	No. of data (n)	54	54	54	54
	Mean (P_m)	1.27	1.25	1.02	1.01
	COV (V_p)	0.210	0.199	0.166	0.166
550°C	No. of data (n)	54	54	54	54
	Mean (P_m)	1.24	1.31	1.00	1.08
	COV (V_p)	0.214	0.204	0.159	0.159
750°C	No. of data (n)	54	54	54	54
	Mean (P_m)	1.24	1.25	1.04	1.02
	COV (V_p)	0.202	0.189	0.187	0.187
900°C	No. of data (n)	54	54	54	54

	Mean (P_m)	1.38	1.33	1.05	0.99
	COV (V_p)	0.170	0.171	0.154	0.154
Overall	No. of data (n)	216	216	216	216
	Mean (P_m)	1.28	1.29	1.03	1.03
	COV (V_p)	0.203	0.192	0.167	0.169
	Resistance factor (ϕ)	1.00	1.00	0.80	0.80
	Reliability index (β_0)	2.23	2.41	2.52	2.50

Table 6. Summary of comparisons between test and FE residual strengths with existing and proposed nominal resistances for RHS X-joints failed by S mode.

Post-fire Temperatures (ψ)	Parameters	Comparisons					
		$\frac{N_{f,\psi}}{N_{E,\psi}}$	$\frac{N_{f,\psi}}{N_{C,\psi}}$	$\frac{N_{f,\psi}}{N_{Lan,\psi}}$	$\frac{N_{f,\psi}}{N_{KL,\psi}}$	$\frac{N_{f,\psi}}{N_{pn1}}$	$\frac{N_{f,\psi}}{N_{pn2}}$
300°C	No. of data (n)	55	55	49	55	55	55
	Mean (P_m)	6.34	4.58	2.37	1.26	1.03	0.95
	COV (V_p)	0.713	0.703	1.006	0.170	0.165	0.166
550°C	No. of data (n)	55	55	49	55	55	55
	Mean (P_m)	5.79	4.23	1.54	1.19	1.06	1.09
	COV (V_p)	0.713	0.694	0.624	0.166	0.157	0.158
750°C	No. of data (n)	55	55	55	55	55	55
	Mean (P_m)	4.90	3.58	1.33	1.13	1.04	1.13
	COV (V_p)	0.695	0.676	0.603	0.155	0.177	0.148
900°C	No. of data (n)	54	54	54	54	54	54
	Mean (P_m)	3.44	2.75	1.07	1.25	1.04	1.08
	COV (V_p)	0.697	0.697	0.306	0.255	0.215	0.224
Overall	No. of data (n)	219	219	207	219	219	219
	Mean (P_m)	5.12	3.79	1.56	1.21	1.04	1.06
	COV (V_p)	0.750	0.725	0.900	0.196	0.179	0.186
	Resistance factor (ϕ)	1.00	1.00	1.00	0.89	0.80	0.80
	Reliability index (β_0)	2.65	2.39	1.02	2.56	2.51	2.54